Langmuir

ARTICLE

pubs.acs.org/Langmuir

Multiparticle Sintering Dynamics: From Fractal-Like Aggregates to Compact Structures

Max L. Eggersdorfer,[†] Dirk Kadau,[‡] Hans J. Herrmann,[‡] and Sotiris E. Pratsinis*[,†]

[†]Particle Technology Laboratory, Institute of Process Engineering, Department of Mechanical and Process Engineering, ETH Zurich, Sonneggstrasse 3, CH-8092 Zürich, Switzerland.

[‡]Computational Physics of Engineering Materials, Institute of Building Materials, Department of Civil, Environmental and Geomatic Engineering, ETH Zurich, Schafmattstrasse 6, CH-8093 Zürich, Switzerland

ABSTRACT: Multiparticle sintering is encountered in almost all high temperature processes for material synthesis (titania, silica, and nickel) and energy generation (e.g., fly ash formation) resulting in aggregates of primary particles (hard- or sinter-bonded agglomerates). This mechanism of particle growth is investigated quantitatively by mass and energy balances during viscous sintering of amorphous aerosol materials (e.g., SiO_2 and polymers) that typically have a distribution of sizes and complex morphology. This model is validated at limited cases of sintering between two (equally or unequally sized) particles, and chains of particles. The evolution of morphology, surface area and radii of gyration of multiparticle aggregates are elucidated for various sizes and initial fractal dimension. For each of these structures that had been generated by diffusion limited (DLA), cluster−cluster (DLCA), and ballistic particle−cluster agglomeration (BPCA) the surface area evolution is monitored and found to scale differently than that of the radius of gyration (moment of inertia). Expressions are proposed for the evolution of fractal dimension and the surface area of aggregates undergoing viscous sintering. These expressions are important in design of aerosol processes with population balance equations (PBE) and/or fluid dynamic simulations for material synthesis or minimization and even suppression of particle formation.

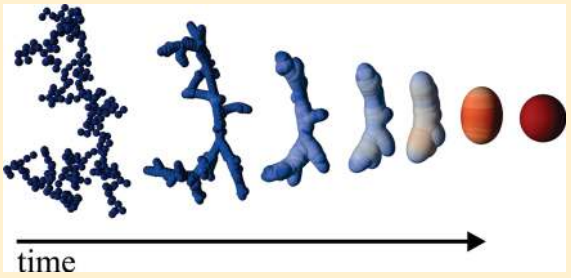

1. INTRODUCTION

Fractal-like aggregates consist of multiple (primary) particles that are connected by chemical (e.g., sintering) bonds. Such aggregates form by natural and man-made processes, typically at high temperatures, like fly ash from volcano eruption and coal combustion as well as aerosol synthesis of pigmentary titania, fumed silica, and carbon black by carefully designed combustion of appropriate liquid or gaseous precursors. The structure of such particles has important implications in their performance. In materials synthesis, for example, structure plays a crucial role in final product performance. In paints, TiO_2 nonaggregated particles (agglomerates) are sought that can be easily dispersed and remain in suspension in liquids. While for catalysts or lightguides, open aggregates are preferred to facilitate gas transport in and out of pellets or preforms. Furthermore, sinter necks are important for the mechanical stability of nanoparticle layers,[1] enhanced electron transport and sensitivity of gas sensors[2] especially when made from narrowly distributed aggregates[3] and electrical conductivity.[4] In design of nanoparticle synthesis by aerosol processes the variation of D_f during particle formation hardly affects the primary particle diameter but is important in determining the collision diameter and in return the aggregate diameter.[5]

Now it is reasonably well understood that such aggregates form by gas and surface reaction, coagulation and partial coalescence (or sintering). As chemical reactions in high temperature aerosol processes are completed much faster than particle dynamics, the detailed structure of these aggregates is largely determined by the interplay of particle collision and coalescence. In the absence of such sintering between primary particles, agglomerates (rather than aggregates) are formed by collision and mere cohesion with well-defined structure and fractal-dimension, D_f, depending only on the particle collision mechanism. For example, agglomerates made by (a) diffusion limited agglomeration (DLA)[6] have $D_f = 2.5$, (b) ballistic particle−cluster agglomeration $D_f = 3.0$ (BPCA),[7] and (c) diffusion limited cluster−cluster agglomeration $D_f = 1.8$ (DLCA).[8] Aggregates may undergo further coagulation leading to formation of agglomerates (physically bonded) that may undergo restructuring and break-up.[9]

Once coalescence or sintering starts between constituent primary particles, sinter necks are formed between them converting the agglomerates to aggregates. During sintering, the latter progressively densify until complete compact (e.g., $D_f = 3$) structures are formed at sufficiently long process times at high temperatures. This has been experimentally demonstrated during silica formation in hot-wall[10] and laminar diffusion flame reactors by small-angle X-ray diffraction.[11] In reality, however, it is rather seldom to have enough process time to complete particle coalescence. As a result,

Received: February 10, 2011
Revised: March 30, 2011

   dx.doi.org/10.1021/la200546g | *Langmuir* XXXX, XXX, 000–000

aggregates are formed with D_f in-between those predicted by particle collision alone (as above) and those for compact particles that underwent full coalescence as has been shown computationally for 2-D structures[12] and experimentally[13] for nanosilica D_f = 1.5−2.4.

The above studies clearly show the need to better understand the variation of D_f during particle synthesis. Essentially one needs to relate the evolution of D_f to that of the characteristic time of sintering. Artelt et al.[5] had proposed a linear relationship between D_f to the characteristic time of sintering. There is however the need to develop such a relation from first principles without adjustable parameters following the detailed evolution of particle structure during sintering. Several models have been proposed for viscous sintering of equally sized pairs of particles.[14−18] Here a new and rather simple model is introduced that describes sintering of two differently sized particles and multiparticle aggregates of amorphous spherical particles (e.g., silica) by mass (or volume)[19] and energy[14] balances. This model reproduces the neck growth and evolution of surface area for equally and differently sized pairs and chains of particles and compared to more detailed sintering model solutions.[20−25] So the evolution of the detailed morphology, radius of gyration and effective fractal dimension of ensembles of irregular particles of arbitrary initial D_f is presented as they asymptotically approach full compactness by coalescence or sintering. Furthermore, simple-to-use expressions for the evolution of these particle characteristics are developed from first principles that are needed[26] in design of nanomaterial synthesis by coagulation and sintering.

2. THEORY

Particle sintering leads to a reduction of free energy by, at least, six distinct physical mechanisms:[27] surface diffusion, bulk diffusion from the surface, vapor transport, grain boundary diffusion, bulk diffusion from the grain boundary, and plastic/viscous flow. All six lead to bonding and neck growth between neighboring particles but only the last three cause densification by approaching particle centers. Viscous sintering is the dominant mechanism for amorphous materials like polymers and glasses[28] and can be described by solving the flow field inside the particles with the Stokes equation.[29] Frenkel[14] developed a geometric sintering model for the initial stage of sintering of spheres by viscous flow. This model has been extended by Eshelby[15] to satisfy the continuity equation and is referred to as the Frenkel−Eshelby model. Here the energy balance of this model is combined with a volume balance model for the initial sintering kinetics of a packed bed of spherical particles.[19] That way a model is developed for two particles that is generalized to multiparticle clusters.

The driving force for sintering is a minimization of the free energy resulting in a reduction of surface area. The energy gained by surface reduction is dissipated by viscous flow, which sets the time scale for sintering. The dissipated energy would increase the particle temperature, which in practical processes is effectively thermostatted or dissipated by the surrounding gas. The flow is assumed to be extensional[14] that results in approaching particle centers so the spherical particles overlap (Figure 1). The overlapping volume is counted only once and in order to conserve particle volume, the particle radius is increased.[19] Moreover the surface energy is assumed to be independent of the primary particle radius, r. The Tolman equation[30] accounts for such an effect for liquid droplets including the ratio δ/r (δ is a constant of the order of intermolecular distance, ~0.1 nm), which is typically small. The present model is designed for amorphous nanoparticles from a few nanometers in diameter up to the micrometer range.

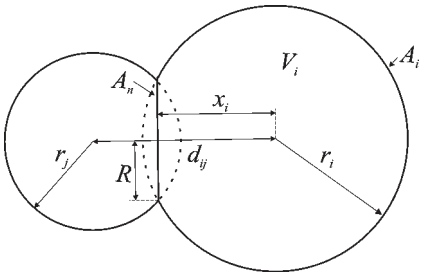

Figure 1. Two-dimensional sketch of a pair of spherical particles during sintering.

2.1. Sintering of Two Particles of Arbitrary Size. *2.1.1. Conservation of Volume.* During particle sintering by viscous flow, particle centers approach each other to reduce their surface area conserving, however, their total volume V

$$\frac{dV}{dt} = \sum_i \frac{dV_i}{dt} = 0 \tag{1}$$

According to Kadushnikov et al.[19] the volume conservation can be written for each individual particle

$$\frac{dV_i}{dt} = \frac{\partial V_i}{\partial r_i}\frac{dr_i}{dt} + \frac{\partial V_i}{\partial x_i}\frac{dx_i}{dt} = 0 \tag{2}$$

with x_i being the distance from the particle center to the neck level and V_i being the spherical particle volume minus the cap volume, Figure 1

$$V_i = \frac{2}{3}\pi {r_i}^3 + \pi {r_i}^2 x_i - \frac{1}{3}\pi {x_i}^3 \tag{3a}$$

$$\text{with } x_i = ({d_{ij}}^2 - {r_j}^2 + {r_i}^2)/(2d_{ij}) \tag{3b}$$

and d_{ij} is the distance between the centers of particles i and j.

The volume balance consists of a loss term, $(\partial V_i/\partial x_i)(dx_i/dt)$, representing the change in volume due to the increasing overlap. The $\partial V_i/\partial x_i$ results in the cross-sectional neck area A_n[31]

$$\frac{\partial V_i}{\partial x_i} = \pi(r_i^2 - x_i^2) = A_n \tag{4}$$

and from eq 3b dx_i/dt is

$$\frac{dx_i}{dt} = \frac{r_i}{d_{ij}}\frac{dr_i}{dt} - \frac{r_j}{d_{ij}}\frac{dr_j}{dt} + \left(1 - \frac{x_i}{d_{ij}}\right)\frac{dd_{ij}}{dt} \tag{5}$$

So the above loss term corresponds to the volume of a cylinder with length dx_i and area A_n. This volume is balanced by the gain term $(\partial V_i/\partial r_i)(dr_i/dt)$, where $\partial V_i/\partial r_i$ determines the free surface area A_i of the sphere

$$\frac{\partial V_i}{\partial r_i} = 2\pi({r_i}^2 + r_i x_i) = A_i \tag{6}$$

Each particle experiences a volume change by an approaching neighboring particle, which is balanced by an increase in the particle radius r_i.[19] So the particle growth rate, dr_i/dt is

$$\frac{dr_i}{dt} = -\left(\frac{\partial V_i}{\partial x_i}\frac{dx_i}{dt}\right)\Big/\frac{\partial V_i}{\partial r_i} = -\frac{A_n}{A_i}\frac{dx_i}{dt} \tag{7}$$

dx.doi.org/10.1021/la200546g |Langmuir XXXX, XXX, 000–000

which is written as a function of the independent variable d_{ij}

$$\frac{dr_i}{dt} = -\frac{A_n\left(\left(1-\frac{x_i}{d_{ij}}\right)-\left(1-\frac{x_j}{d_{ij}}\right)\cdot\frac{A_n r_j/d_{ij}}{A_j - A_n r_j/d_{ij}}\right)}{\left(A_i - \frac{A_n r_i}{d_{ij}} - \frac{A_n r_j}{d_{ij}}\cdot\frac{A_n r_i/d_{ij}}{A_j - A_n r_j/d_{ij}}\right)}$$

$$\frac{dr_i}{dt} = B_i\frac{dd_{ij}}{dt} \tag{8}$$

where B_i represents the elaborate fraction for simplicity.

2.1.2. Conservation of Energy. The Frenkel−Eshelby model was derived on the basis of an energy balance which equals the energy gained by surface reduction to the energy dissipated by a uniaxial extensional flow under the assumption of constant particle radius and small angles, which is valid for the initial sintering stage. Pokluda et al.[18] extended the Frenkel−Eshelby model to describe the complete sintering of two equally sized spherical particles. Here this is extended to differently sized particles by a more general derivation of the rate of change of surface area, dA_i/dt. This is important for aerosol particles that have typically a distribution of sizes and complex morphology. The change in surface energy equals the viscous dissipation with the assumption of a constant strain rate ε inside the whole particle[14]

$$-\gamma\frac{dA_i}{dt} = \iiint 3\eta\dot{\varepsilon}_i^2\, dV_i = 3\eta V_i\dot{\varepsilon}_i^2 \tag{9}$$

where γ is the surface energy and η the viscosity. The strain rate is approximated as[18]

$$\dot{\varepsilon}_i = \frac{1}{r_i}\frac{dx_i}{dt} \tag{10}$$

Similar to volume conservation (eq 2), the change in surface area, dA_i/dt, is split into a gain and loss term

$$\frac{dA_i}{dt} = \frac{\partial A_i}{\partial r_i}\frac{dr_i}{dt} + \frac{\partial A_i}{\partial x_i}\frac{dx_i}{dt} \tag{11}$$

The approaching neighboring particle reduces the surface (loss term), which is counteracted by an increase in the particle radius (gain term). The free surface area of a particle with one contact is

$$A_i = 4\pi r_i^2 - 2\pi r_i(r_i - x_i) = 2\pi(r_i^2 + r_i x_i) \tag{12}$$

The partial derivatives of A_i with respect to x_i and r_i are

$$\frac{\partial A_i}{\partial x_i} = 2\pi r_i \text{ and } \frac{\partial A_i}{\partial r_i} = 4\pi r_i + 2\pi x_i \tag{13}$$

Combining eqs 5 and 8−13 results in a system of equations that describes the full coalescence of two spherical particles of arbitrary size ratio, the change in distance dd_{ij}/dt and the change in particle radius dr_i/dt

$$\frac{dd_{ij}}{dt} = -\frac{4r_i r_j d_{ij}^2(r_i + r_j)\gamma}{(r_i + r_j + d_{ij})(r_i^4 + r_j^4 - 2r_i^2 r_j^2 + 4d_{ij}r_i r_j(r_i + r_j) - d_{ij}^2(r_i^2 + r_j^2))\eta} \tag{14a}$$

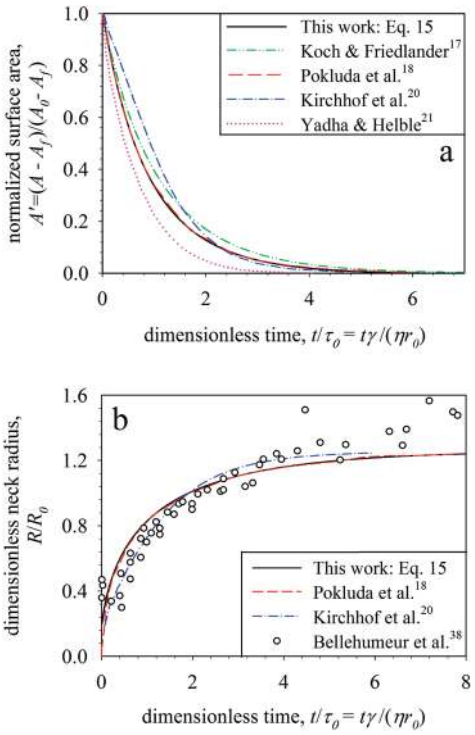

Figure 2. Evolution of (a) normalized surface area A' and (b) dimensionless neck radius R/R_0 for two equally sized spheres undergoing sintering. The model of Pokluda et al.[18] gives identical results as the present work (a and b) as both models are based on the energy equation of the Frenkel-Eshelby model but use a different derivation and representation of dA/dt. The work of Kirchhof et al.[20] predicts at the beginning of sintering a slower change in surface area than the present work as well as with Koch and Friedlander,[17] Pokluda et al.,[18] and Yadha and Helble.[21] At the end of sintering, the change in surface area is faster in the model of Yadha and Helble[21] than the other, which are in reasonable agreement with the present work. (b) Good agreement in the predicted neck radius is found between the present work and both simulations[20] and experiments of polymer sintering.[38]

$$\frac{dr_i}{dt} = B_i\frac{dd_{ij}}{dt} \tag{14b}$$

For two equally sized particles ($r_i = r_j$, $d_{ij} = 2x_i$) the sintering equations reduce to

$$\frac{dd_{ij}}{dt} = \frac{4r_i d_{ij}\gamma}{(2r_i + d_{ij})(d_{ij} - 4r_i)\eta} \tag{15a}$$

$$\frac{dr_i}{dt} = \frac{(d_{ij} - 2r_i)d_{ij}\gamma}{2(2r_i + d_{ij})(d_{ij} - 4r_i)\eta} \tag{15b}$$

Pokluda et al.[18] already derived a viscous sintering equation for two equally sized particles. Equation 15 can be compared to their equation, if $d_{ij} = 2r_i\sin(\theta)$ is applied. The dd_{ij}/dt of eq 15a is transformed to $d\theta/dt = \gamma 2^{-5/3}\cos(\theta)\sin(\theta)(2 - \cos(\theta))^{1/3}/(a_0\eta(1 - \cos(\theta))(1 + \cos(\theta))^{1/3})$, which is the sintering equation of Pokluda et al.,[18] Figure 2. The advantage of using the distance d_{ij} as the independent variable instead of the angle θ is that it can be used for unequally sized particles and multiparticle sintering.

The present model is developed for viscous sintering of amorphous particles. Sintering of crystalline materials can be

dx.doi.org/10.1021/la200546g |*Langmuir* XXXX, XXX, 000–000

simulated with the present model by replacing the energy balance of eq 9 to account for the different physics. For example for grain boundary diffusion, typically used to describe the sintering of TiO_2 particles,[32] the change in volume with respect to approaching particle centers equals the diffusion of atoms from the grain boundary to the neck:

2.2. Multiparticle Sintering. The above two-particle model is extended to multiparticle sintering of chains and irregular structures. Each particle can have now several neighbors. The volume displaced by the reduction of particle distance equals the volume gained by increasing the radius:

$$\frac{dV_i}{dt} = \frac{\partial V_i}{\partial r_i}\frac{dr_i}{dt} + \sum_j \frac{\partial V_i}{\partial x_{i,j}}\frac{dx_{i,j}}{dt} = 0 \qquad (16)$$

where the sum is taken over all j neighbors of particle i. For multiple particle overlaps the neck area is no longer circular. Therefore the particle surface area, volume, neck areas, and neighbors are calculated with the Vorlume software.[33] It is an exact method which decomposes the volume of the union of spheres into convex regions, namely the restrictions of the spheres. The calculation of a restriction volume is based on Gauss' divergence theorem.[34]

Kirchhof et al.[20] found that the single sintering necks are independent from each other by solving the flow field inside the particles with a fractional volume of fluid method. The new particle positions are obtained by a SHAKE algorithm[35] to fulfill the constraints of the relative distances to the neighbor particles up to a tolerance of 0.1% or 1000 iterations. The SHAKE method reduces the particle distances according to eq 14a. This allows simulating the restructuring of the whole aggregate. For example, the motion of an edge in a chain is the sum of all displacements of the intermediate particles. This is accounted for by the iterative solution of the new particle positions.

In reality, aggregates are highly irregular consisting usually of several (up to hundreds) of primary particles.[13] The effective fractal dimension D_f is used to describe the morphology of irregularly shaped aggregates[36]

$$N = k_f\left(\frac{R_g}{r_0}\right)^{D_f} \qquad (17)$$

where N is the number of primary particles in the aggregate, k_f a prefactor, and R_g the radius of gyration[37]

$$R_g{}^2 = \frac{\int \rho(r) r^2 \, dr}{\int \rho(r) \, dr} \qquad (18)$$

where $\rho(r)$ is the radial density distribution function.

3. RESULTS AND DISCUSSION

3.1. Validation. *3.1.1. Two-Particle Sintering: Equally-Sized Particles.* First, the two-particle sintering model of eq 15 is validated with simulations[17,18,20,21] and experiments.[38] Figure 2 shows the evolution of the normalized surface area (a) and dimensionless neck radius (b). The present results for equally sized particles (solid line) are identical to those (broken line) of Pokluda et al.[18] as both models use the energy equation of Frenkel[14] but a different solution representation. Initially the change in surface area is very rapid and almost linear, as the classic model of Frenkel-Eshelby predicts. At the beginning, the difference in curvatures in the neck region and therefore the pressure toward a reduction of the surface area are highest. There, the present model (eq 15, solid line) is closer to that of Yadha and Helble[21] (dotted line) and Koch and Friedlander[17] (double-dot broken line) than those of Kirchhof et al.[20] (dash-dot line). Koch and Friedlander[17] proposed (KF model):

$$\frac{dA}{dt} = -\frac{1}{\tau_A}(A - A_f) \qquad (19)$$

where τ_A is the characteristic fusion time, A the aggregate surface area, and A_f its final value upon complete coalescence. Koch and Friedlander[17] used a phenomenological fusion time of $\tau_A = \eta r_{mono}/\gamma$ for two equally sized particles, with $r_{mono} = 3V/A$ being the equivalent radius of monodisperse spherical primary particles at each time step.[39] Equation 19 can be solved analytically, $A(t) = A_f/(1 - (1 - (A_f/A_0))\exp(-((\gamma A_f)/(3\eta V)t)))$, with the initial condition $A(t = 0) = A_0$. The present work is in good agreement with the KF model for two equally sized particles (Figure 2). The dA/dt differ at the beginning of sintering by about 20% and converge both to zero for $A \rightarrow A_f$ (Appendix). If the characteristic fusion time is constant ($\tau_A = \eta r_0/\gamma$), the normalized surface area decreases exponentially

$$A' = (A - A_f)/(A_0 - A_f) = \exp(-t/\tau_A) \qquad (20)$$

Figure 2b shows the evolution of the dimensionless neck radius R/R_0 with dimensionless time t/τ_0. The neck radius increases rapidly at the initial sintering stage and levels off slowly at later times since the whole sintering process slows down as its driving force (particle curvature) decreases. Experimental data of Bellehumeur et al.[38] (symbols) for sintering of irregular and cylindrically shaped polyethylene particles with a size distribution between 250 to 600 μm match well with the present model as well to that by Pokluda et al.[18] (dotted line). The large deviations at the late stage of the experiments come from the loss of 3-D structure as particles spread on the observation surface.[18] An even better match is obtained by Kirchhof et al.[20] (dash-dot line) indicating further that viscous sintering is the dominant mechanism in these experiments. Nonetheless the volume of fluid method needs a high discretization of the particle volume and is computationally demanding.[20]

3.1.2. Two-Particle Sintering: Differently-Sized Particles. Figure 3a shows the evolution of the dimensionless surface area A/A_0 for various particle radii ratios ($r_{1,0}/r_{2,0} = 1-6$) by the present model (lines) and that of Yadha and Helble[21] (symbols). Similar to the sintering of equally sized particles (Figure 2a), Yadha and Helble[21] predict faster sintering. They found that the coalescence times of unequally sized particles did not scale linearly with the radii ratio, nor with the total volume of the two particles and concluded that sintering time depends primarily on the size of the smaller particle. Here, a scaling is identified which collapses the normalized surface area evolution by particles of various size ratios nearly onto a single curve, if the dimensionless time is scaled with the time dependent radius of the smaller particle $r(t)$, Figure 3b. Additionally good agreement is found between the present work (eq 14) and the KF model (eq 19), if the radius in the fusion time, $\tau_A = \eta r(t)/\gamma$, is chosen as the smaller particle's radius. The smaller particle dominates the sintering process consistent with FEM,[40] CFD,[20,21] and MD[41] simulations.

dx.doi.org/10.1021/la200546g |Langmuir XXXX, XXX, 000–000

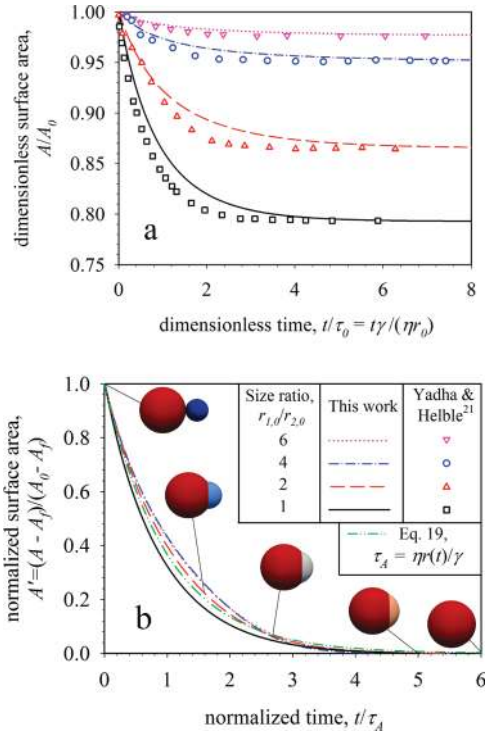

Figure 3. Temporal evolution of (a) dimensionless A/A_0 and (b) normalized surface area A' by the present work (lines) and by Yadha and Helble[21] (symbols) for pairs of particles with size ratios $r_{1,0}/r_{2,0}$ = 1−6. If the time is scaled with the radius of the small particle $r(t)$, the evolution of A' collapses around a single line described well by an exponential model (double-dot broken line) with the proposed fusion time $\tau_A = \eta r(t)/\gamma$. The colors of the inset particles correspond to their large (blue) and small (red) curvature (= 1/radius).

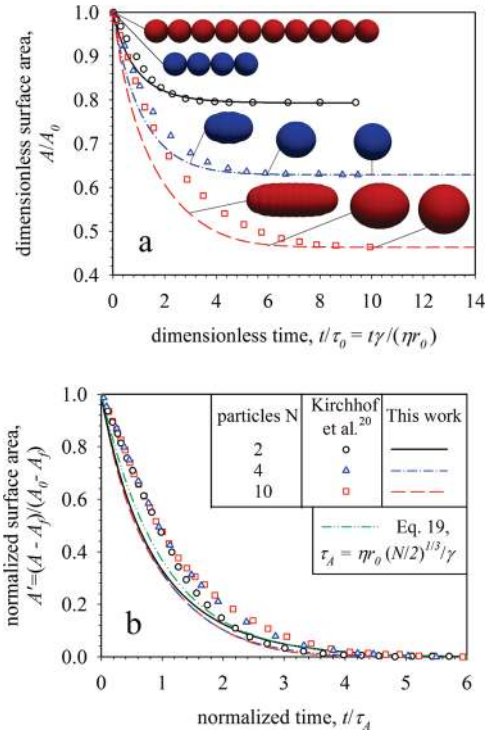

Figure 4. (a) Evolution of the dimensionless surface area A/A_0 of chain aggregates by the present work (lines) and by Kirchhof et al.[20] (symbols). The characteristic size in the dimensionless time is the primary particle radius r_0. The present work predicts faster sintering than Kirchhof et al.,[20] which comes from the difference in two-particle sintering. Nevertheless the scaling proposed by Kirchhof et al.[20] is also valid here collapsing the change in surface area around a single curve (b) if the time is scaled by the characteristic fusion time $\tau_A = \eta r_0 (N/2)^{1/3}/\gamma$. Additionally the Koch and Friedlander[17] model (eq 19, double-dot broken line) describes the surface area evolution well compared to the present work.

3.1.3. Multiparticle Sintering of Particle Chains. Figure 4 shows the sintering of chain aggregates consisting of 2−10 monodisperse primary particles as simulated by the present multiparticle sinter model (eq 14 and 16, lines) and compared to that (symbols) of Kirchhof et al.[20] The chain aggregate shrinks and forms an oval shape by further densification and becomes finally spherical.[25] Figure 4a shows the evolution of the total surface area A normalized by the initial surface area A_0. Longer chains take more time to sinter as expected. The present model predicts slightly faster sintering (10−15%) than Kirchhof et al.[20] as already seen in Figure 2b, but properly converges to the asymptotic result. Kirchhof et al.[20] suggested to scale the time with the equivalent radius of the fully coalesced sphere, $r_f = N^{1/3} r_0$, to collapse the normalized surface areas onto one single curve. Figure 4b shows that the evolution of normalized surface area from 2 to 10 particle chains by the present model scales slightly better than the data of Kirchhof et al.[20] (symbols). Again the initial sintering stage is almost linear but can be described reasonably well by the KF model (eq 19, double-dot broken line) where instead of the primary particle radius, $(N/2)^{1/3} r_0$ is used for the characteristic fusion time τ_A. The various symmetric structures consisting of ten particles each investigated by Kirchhof et al.[20] have been studied as well with similar results as above (not shown here). The fastest sintering occurred for the most compact structure.

3.2. Aggregate Dynamics. *3.2.1. Multiparticle Sintering of Irregular Aggregates.* All results shown until here have been deterministic. For irregular particle structures the results are averaged over 50 different aggregates for each structure specification. The morphology of flame-generated silica or titania aggregates range typically from D_f = 1.5 to 2.4.[13,42] A D_f of around 1.8 corresponds to open structured aggregates generated by diffusion-limited cluster−cluster agglomeration (DLCA).[8] The D_f larger than 1.8 can be attributed to aggregate sintering.[11] Although the dominant aggregation mechanism for particles produced in flames is DLCA, the influence of different initial aggregate morphologies is studied here as well. The evolution of the dimensionless and normalized surface area, the radius of gyration and the effective fractal dimension is presented and the influence of the number of particles and initial aggregate structure is investigated here.

Agglomerates of 16−512 primary particles are produced by diffusion-limited hierarchical cluster−cluster (DLCA),[43] diffusion limited (DLA),[6] and ballistic particle−cluster (BPCA)[7] agglomeration. The DLA and BPCA agglomerates are only created to investigate here the effect of the initial morphology. An estimate of the initial D_f is obtained by ensemble averaging over 50 aggregates of each size using the radius of gyration and eq 17 to validate agglomerate generation and compare to the estimated values known from literature. The aggregates studied here might be too small to obtain a strict scaling over several orders of magnitude and therefore the fitted D_f has to be

dx.doi.org/10.1021/la200546g |*Langmuir* XXXX, XXX, 000–000

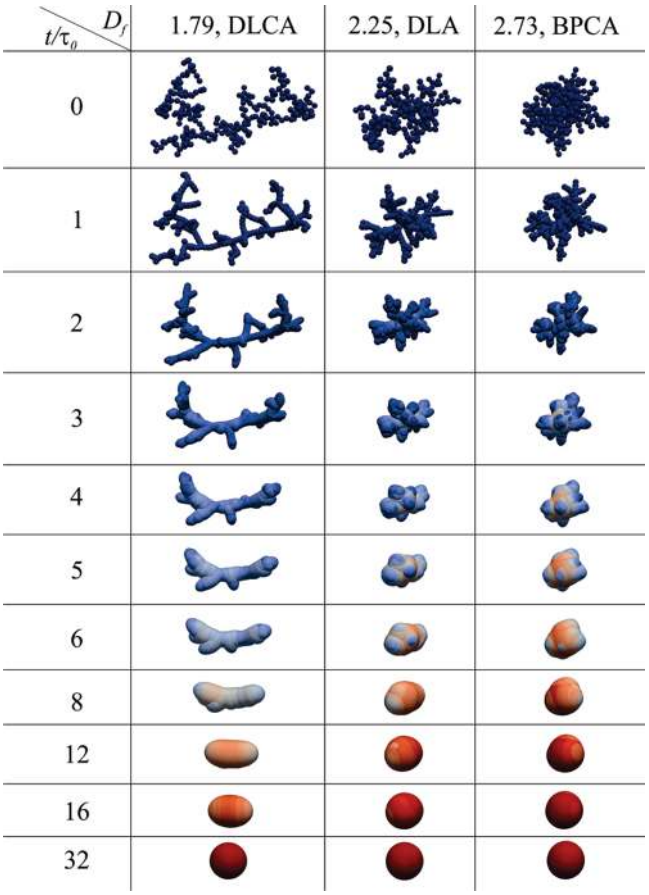

Figure 5. Snapshots of aggregates undergoing viscous sintering and consisting of initially 256 monodisperse primary particles generated by diffusion limited cluster−cluster (DLCA, D_f = 1.79), diffusion limited (DLA, D_f = 2.25), and ballistic particle-cluster (BPCA, D_f = 2.73) agglomeration. Clearly compact aggregates sinter faster than more open structures. The dimensionless time, $t/\tau_0 = t\gamma/\eta r_0$, is listed next to the aggregate. The colors correspond to the aggregate curvature (= 1/radius): large = blue, small = red.

considered as an estimate or an effective, strictly speaking. The experimentally investigated SiO_2 particles/aggregates produced in flames consist of a similar size (1−1000 primary particles) depending on process conditions.[10,11,13] The DLCA clusters made here have a $D_f = 1.79 \pm 0.03$ and $k_f = 1.39 \pm 0.06$, consistent with Sorensen and Roberts.[44] The obtained error bars correspond to the standard error of regression (standard deviation divided by square root of number of aggregates). The fractal dimension and prefactor of clusters generated by DLA are $D_f = 2.25 \pm 0.03$ and $k_f = 0.82 \pm 0.05$ and of BPCA are $D_f = 2.73 \pm 0.03$ and $k_f = 0.538 \pm 0.05$, respectively. These D_f are lower than their asymptotic values of 2.5 and 3 for DLA and BPCA agglomeration, respectively, as the D_f of small clusters is lower than their asymptotic.[45]

Figure 5 shows the viscous sintering of aggregates originally made by DLCA, DLA, and BPCA with initial D_f of 1.79, 2.25, and 2.73, respectively, consisting of 256 primary particles each. At the beginning of sintering, the aggregate branches straighten and broaden (dimensionless time $t/\tau_0 = 1$) resulting in more open structures, as discussed below with the evolution of D_f. This is contradictory to the general notion that sintering leads automatically to compaction. This is consistent, however, with Akhtar et al.,[12] who observed in 2-dimensional Monte Carlo simulations of gas phase coagulation and sintering of TiO_2 aerosol that the densification on a localized scale of the branches in the aggregates leads to a reduction in D_f. This is consistent also with Camenzind et al.,[11] who experimentally observed a reduction of D_f of silica particle formation in diffusion flame aerosol reactors. At the more densely populated parts of the aggregates, a single compact primary particle is formed ($t/\tau_0 = 1-2$), resulting in more open structures. The branches sinter and the chain diameter increases until an oval shape is reached (t/τ_0 = 12, DLCA) which finally evolves to a spherical particle.

The shape evolution of the DLA aggregate is comparable to that of the DLCA aggregate. After chains have straightened ($t/\tau_0 = 1$), the DLA aggregate forms an elongated shape ($t/\tau_0 = 2-6$), yet more compact than the DLCA aggregate. The BPCA aggregate behaves differently after chains have straightened (t/τ_0 = 1). Rapidly a dense center is formed in the aggregate into which the branches sinter ($t/\tau_0 = 2-5$). At the end of sintering ($t/\tau_0 > 6$) the surface is smoothened similar to the DLCA aggregate. The influence of the initial structure on the evolution of surface area and radii of gyration are quantitatively studied below.

3.2.2. Effect of the Number of Primary Particles per Agglomerate on its Sintering. Figure 6a shows the temporal evolution of the dimensionless surface area A/A_0 for DLCA aggregates consisting of 16−512 primary particles. The highlighted area represents the range of the standard deviation averaged over the 50 aggregates. At the beginning, the change is very rapid and almost independent of the number of particles in the aggregate. This change in surface area corresponds to the initial neck formation, which comes along with a great reduction in surface area and is much faster than at the end of sintering. The reason is the large difference in curvatures in the neck as seen for two-particle sintering (Figure 2). The normalized surface areas collapse around a single line up to $A' = 0.2$ (Figure 6b), if the time is scaled with

$$\tau_A = \frac{\eta r_0}{\gamma}\left(\frac{N}{2}\right)^{(1/2 - D_f/6)} \quad (21)$$

which corresponds to the characteristic fusion time for the KF model (eq 19). This time can be used in population balance equations (PBE) to predict the evolution of the particle surface area as a function of particle number and initial effective fractal dimension.

The evolution of the radius of gyration is presented in Figure 6c. At the beginning of sintering, each branch in the aggregate straightens by shrinking and smoothens the surface area, which does not change the radius of gyration and develops cylinder-like branches (Figure 5). Then the branches shrink like the chains studied above. The temporal evolution of the radius of gyration scales best with $N^{(0.7-0.18D_f)}$, (Figure 6d). Figure 6, panels a and c, shows that the change in surface area takes place faster than the change in radius of gyration. At t/τ_0 = 10, the surface area for N = 512 particles (pink line) was reduced to around 90% of the difference between the initial surface and the fully coalesced sphere, while the R_g has changed to about 70%.

Note that the surface area scales differently than the radius of gyration. The scaling for the radius of gyration (or moment of inertia as often measured in MD simulations) insufficiently describes the surface area evolution and both evolutions need to be considered separately in calculating the collision frequency of aggregate particles undergoing coagulation.

dx.doi.org/10.1021/la200546g |*Langmuir* XXXX, XXX, 000–000

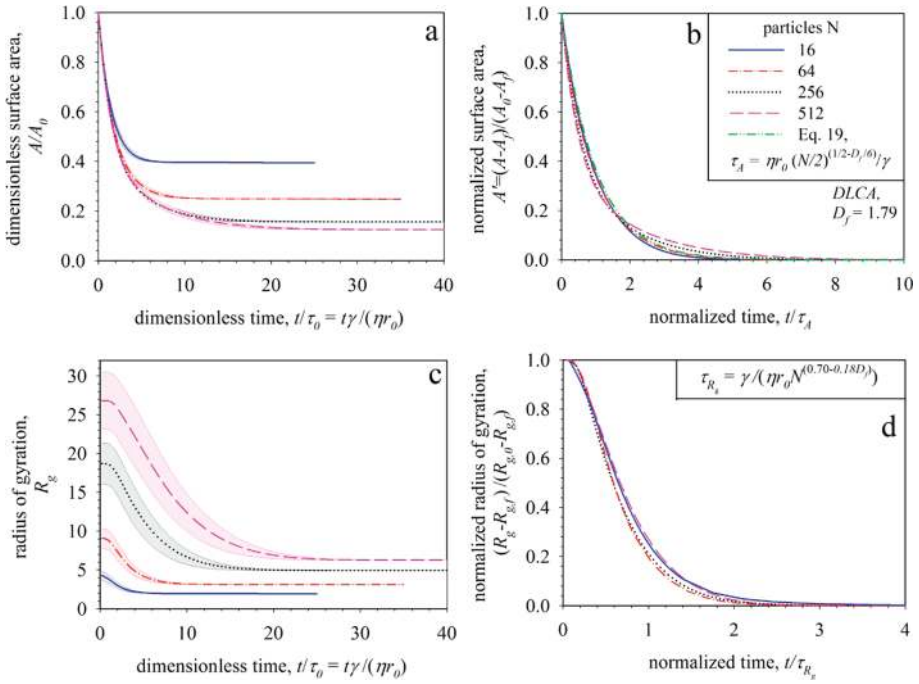

Figure 6. Evolution of dimensionless and normalized surface area (a,b) and radius of gyration R_g (c,d) of DLCA aggregates (initial $D_f = 1.79$) consisting of 16−512 monodisperse primary particles. The results are averaged over 50 different aggregates of each size and the highlighted areas in (a) and (c) represent the range of the standard deviation. The more primary particles an aggregate has, the longer it takes until the particles fully coalesce. If the time is scaled with $\tau_A = \eta r_0 (N/2)^{(0.5-D_f/6)}/\gamma$, the normalized surface area evolution collapses around a single line up to $A' = 0.2$ (b) and is described well by the KF model (eq 19). (d) The evolution of the normalized radius of gyration scales best with $N^{(0.7-0.18D_f)}$. The surface area evolution scales differently than that of the radius of gyration (or moment of inertia).

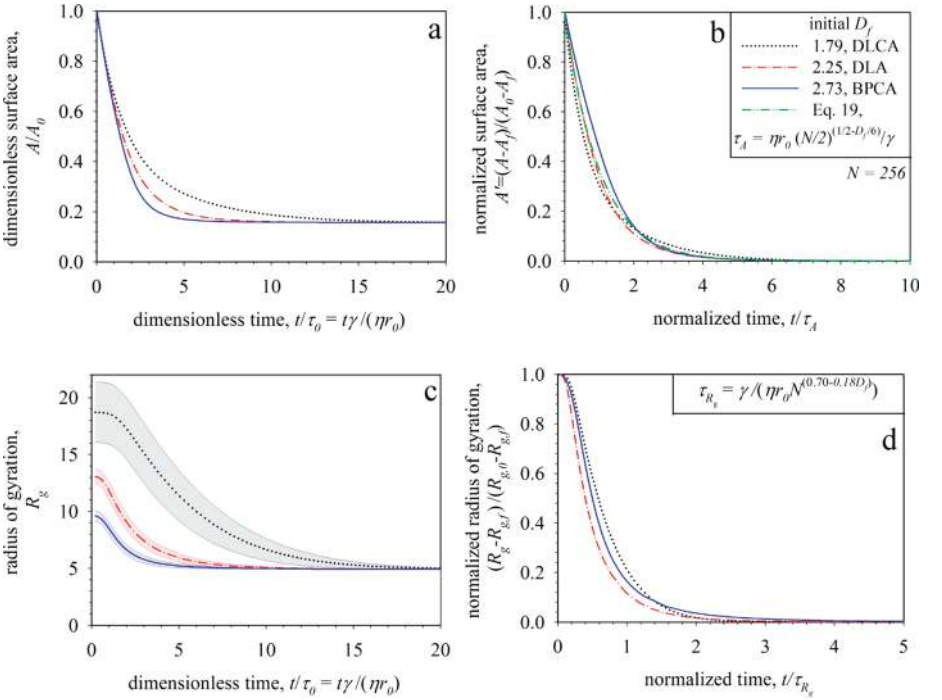

Figure 7. Evolution of dimensionless and normalized surface area (a,b) and radius of gyration (c,d) for DLCA ($D_f = 1.79$), DLA ($D_f = 2.25$), and BPCA ($D_f = 2.73$) agglomerates consisting initially of 256 primary particles. The results are averaged over 50 different aggregates of each structure and the highlighted areas in (c) represent the range of the standard deviation. If the time is scaled with $\tau_A = \eta r_0 (N/2)^{(0.5-D_f/6)}/\gamma$, the normalized surface area evolution collapses around a single line (b) and is described well (within 10%) by the KF model (eq 19). (d) The evolution of the radius of gyration scales best with $N^{(0.7-0.18D_f)}$. The surface area evolution scales differently than that of the radius of gyration (or moment of inertia).

dx.doi.org/10.1021/la200546g |*Langmuir* XXXX, XXX, 000–000

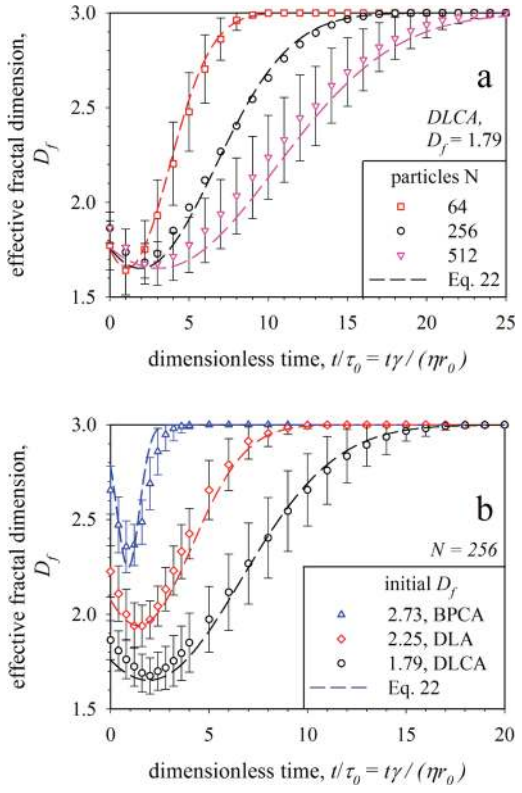

Figure 8. (a) Evolution of the effective fractal dimension is shown for DLCA aggregates undergoing sintering and consisting of 64−512 primary particles. Initially, all aggregates are becoming more open as the branches straighten. (b) Temporal evolution of the effective fractal dimension D_f for initially DLCA (D_f = 1.79), DLA (D_f = 2.25), and BPCA (D_f = 2.73) agglomerates consisting of 256 primary particles. The DLCA aggregates are more elongated and take more time to reach both the minimum in D_f and full coalescence. Equation 22 describes the structural changes during viscous sintering independent of the number of particles N (a) or the initial D_f (b). The results (a and b) are averaged over 50 different aggregates of each size/structure and the error bars represent the range of the standard deviation.

3.2.3. Effect of Initial Morphology or Structure on Aggregate Sintering. Figure 7 shows the influence of initial aggregate morphology or structure on the surface area evolution and radius of gyration. Initial effective fractal dimensions of 1.79 (DLCA), 2.25 (DLA), and 2.73 (BPCA) are investigated for aggregates consisting of 256 primary particles. The clear trend that more compact aggregates sinter faster can be seen in both the surface area and radius of gyration (Figure 7, panels a and c). Figure 7b shows the change in surface area normalized by the characteristic fusion time introduced above. All evolutions of A' collapse around a single line. The KF model (eq 19) with this τ_A describes the surface area evolution well (within 10%) compared to present simulations using the proposed characteristic fusion time here (eq 21).

The radius of gyration scaling is again different than that of the surface area for various initial morphologies (Figure 7d). For PBE accounting for coagulation and sintering, the evolution of the surface area and collision radius play a crucial role to calculate collision frequencies and of course to predict the surface area of the final product powder and the average particle size.

3.2.4. Evolution of Effective Fractal Dimension, D_f. The D_f is estimated with the sandbox method[36] assuming that a power law between mass and size exists, at least within certain length scales, and serves as a quantitative measure of aggregate structure. The D_f is calculated for each individual aggregate separately and the error bars correspond to the standard deviation from averaging over 50 aggregates. Figure 8a shows the temporal evolution of the effective fractal dimension D_f for DLCA aggregates. For clarity, error bars are shown only for the largest (512 particles) and smallest (64 particles) aggregates. At the beginning of sintering (Figure 5, at t/τ_0 = 1) the highly ramified aggregate branches straighten when primary particles approach each other (reduction of center-to-center distance). This internal restructuring practically unfolds the aggregate and D_f is reduced. However the branches continue shrinking while conserving mass. Further downstream D_f increased as aggregates compacted by sintering-coalescence consistent with in situ measurements by small-angle X-ray scattering (SAXS)[11] as discussed with Figure 5 where individual chains in an aggregate straighten and its structure becomes initially more open or at least does not change significantly.

Equation 22 is proposed to describe the temporal evolution of D_f that properly converges to D_f = 3 exponentially and goes through a minimum at $t_{min} = -C_2\eta r_0/\gamma$ and $D_f = 3 - C_1$. The reduction and increase in D_f is fairly symmetric and each curve has a characteristic width (C_3). The variables C_1, C_2, and C_3 are determined by fitting to each curve of Figure 8 and are finally linearly interpolated

$$D_f(t) = 3 - C_1 \exp\left(-\left(\left(\frac{t\gamma}{\eta r_0} + C_2\right)/C_3\right)^2\right) \qquad (22)$$

with $C_1 = 2.5-0.64D_{f,0}$, $C_2 = 1.1D_{f,0} - 0.0044N - 2.77$, and $C_3 = 0.015N - 6.3D_{f,0} + 14.16$.

Different initial D_f are investigated for 256 primary particle aggregates in Figure 8b. Initially more compact aggregates reach the minimum in D_f and full coalescence faster. Moreover with eq 22 the effective fractal dimension can be determined at any time during the sintering process of irregular aggregates with initially monodisperse primary particles.

4. CONCLUSIONS

Sintering of fractal-like aggregates of primary particles is simulated by a model conserving energy and particle mass. The change in surface energy equals the energy dissipated by the viscous flow. Aggregate densification is driven by the reduction of surface area. The two-particle version of this model is in good agreement with more elaborate simulations and experiments for particle pairs. It is shown that the assumption of an exponential reduction in surface area[17] fits well for both equally and differently sized particles. With the complete model multiparticle sintering is simulated and validated against fractional volume of fluid simulations for chain aggregates. The evolution of the normalized surface area, radius of gyration and effective fractal dimension during sintering is presented for aggregates of initial D_f = 1.79−2.73 made by various collision mechanisms. A new characteristic fusion time is proposed which can be applied to the Koch and Friedlander[17] model for aggregate surface area evolution. At limiting cases this reduces nicely to sintering of two particles (N = 2) and chain agglomerates (D_f = 1). Furthermore the evolution of radius of gyration (or moment of inertia) scales differently than the surface area evolution. Finally from the present detailed simulations, an equation is developed describing

dx.doi.org/10.1021/la200546g |*Langmuir* XXXX, XXX, 000–000

the evolution of the effective fractal dimension D_f during viscous sintering or coalescence that is consistent with experimental observations.

7. APPENDIX

7.1. Analytical Comparison between the Koch and Friedlander[17] Model and This Work. Equation 15 is transformed to dA/dt to facilitate comparison to the KF[17] model

$$\frac{dA}{dt} = \frac{\pi\gamma}{\eta}\frac{{d_{ij}}^2}{d_{ij} - 4r_i} \tag{A1}$$

with r_i being the analytical formula for the radius at d_{ij} to conserve mass for two equally sized particles

$$r_i = \frac{1}{4}(64{r_0}^3 + {d_{ij}}^3 + 8\sqrt{64{r_0}^6 + 2{r_0}^3{d_{ij}}^3})^{1/3} + \frac{1}{4}\frac{{d_{ij}}^2}{(64{r_0}^3 + {d_{ij}}^3 + 8\sqrt{64{r_0}^6 + 2{r_0}^3{d_{ij}}^3})^{1/3}} - \frac{1}{4}d_{ij} \tag{A2}$$

The KF model is written for a constant fusion time $\tau_0 = \eta r_0/\gamma$ as a function of the independent variables d_{ij} and r_0 with r_i replacing the elaborate analytical term

$$\frac{dA}{dt} = -\frac{1}{\tau_f}(A - A_f) = -\frac{4\pi\gamma}{\eta r_0}\left({r_i}^2 + \frac{1}{2}r_i d_{ij} - 2^{2/3}{r_0}^2\right) \tag{A3}$$

or with the time dependent fusion time $\tau_A = 3\eta V/\gamma A$

$$\frac{dA}{dt} = -\frac{16\pi\gamma r_i(-2{r_i}^2 - r_i d_{ij} + 2^{5/3}{r_0}^2)}{\eta({d_{ij}}^2 - 2r_i d_{ij} - 8{r_i}^2)} \tag{A4}$$

Although the dependencies in eq A1, A3, and A4 of dA/dt on d_{ij} and r_0 differ, the numerical values are initially within 20% and converge both to zero at the end of sintering. Equation A3 with a constant sinter time compares better to this work, not shown here.

AUTHOR INFORMATION

Corresponding Author

*Ph.: +41 (0) 44 632 31 80. Fax: +41 (0) 44 632 15 95. E-mail: pratsinis@ptl.mavt.ethz.ch.

ACKNOWLEDGMENT

Financial support by ETH Research Grant (ETHIIRA) ETH-11 09-1 and the European Research Council is gratefully acknowledged.

NOMENCLATURE

A	area, m^2
B	auxiliary variable for eq 8
$C_{1/2/3}$	fitting variables for eq 22
D_f	effective fractal dimension
d	distance between particle centers, m
k_f	prefactor of fractal scaling law
N	number of primary particles
R	neck radius, m
R_g	radius of gyration, m
r	radius, m
t	time, s
V	volume, m^3
x	particle center to neck distance, m

Greek Letters

γ	surface energy, kg s^{-2}
ε	strain rate, s^{-1}
η	viscosity, kg m^{-1} s^{-1}
ρ	density, kg m^{-3}
τ	characteristic time, s

SUBSCRIPTS

0	initial
A	surface area
f	final
i	particle index
j	neighbor index
min	minimum
mono	monodisperse
n	neck
R_g	radius of gyration

REFERENCES

(1) Tricoli, A.; Graf, M.; Mayer, F.; Kuhne, S.; Hierlemann, A.; Pratsinis, S. E. *Adv. Mater.* **2008**, *20*, 3005–3010.
(2) Tricoli, A.; Graf, M.; Pratsinis, S. E. *Adv. Funct. Mater.* **2008**, *18*, 1969–1976.
(3) Keskinen, H.; Tricoli, A.; Marjamaki, M.; Makela, J. M.; Pratsinis, S. E. *J. Appl. Phys.* **2009**, *106*, 084316.
(4) Riefler, N.; Madler, L. *J. Nanopart. Res.* **2010**, *12*, 853–863.
(5) Artelt, C.; Schmid, H. J.; Peukert, W. *J. Aerosol Sci.* **2003**, *34*, 511–534.
(6) Witten, T. A.; Sander, L. M. *Phys. Rev. Lett.* **1981**, *47*, 1400–1403.
(7) Sutherland, D. N. *J. Colloid Interface Sci.* **1966**, *22*, 300–302.
(8) Kolb, M.; Herrmann, H. J. *Phys. Rev. Lett.* **1987**, *59*, 454–457.
(9) Eggersdorfer, M. L.; Kadau, D.; Herrmann, H. J.; Pratsinis, S. E. *J. Colloid Interface Sci.* **2010**, *342*, 261–268.
(10) Seto, T.; Hirota, A.; Fujimoto, T.; Shimada, M.; Okuyama, K. *Aerosol Sci. Technol.* **1997**, *27*, 422–438.
(11) Camenzind, A.; Schulz, H.; Teleki, A.; Beaucage, G.; Narayanan, T.; Pratsinis, S. E. *Eur. J. Inorg. Chem.* **2008**, 911–918.
(12) Akhtar, M. K.; Lipscomb, G. G.; Pratsinis, S. E. *Aerosol Sci. Technol.* **1994**, *21*, 83–93.
(13) Scheckman, J. H.; McMurry, P. H.; Pratsinis, S. E. *Langmuir* **2009**, *25*, 8248–8254.
(14) Frenkel, J. *J. Phys. (USSR)* **1945**, *9*, 385–391.
(15) Eshelby, J. D. *Metals Trans.* **1949**, *185*, 806–807.
(16) Rumpf, H.; Sommer, K.; Steier, K. *Chem. Ing. Tech.* **1976**, *48*, 300–307.
(17) Koch, W.; Friedlander, S. K. *J. Colloid Interface Sci.* **1990**, *140*, 419–427.
(18) Pokluda, O.; Bellehumeur, C. T.; Vlachopoulos, J. *AIChE J.* **1997**, *43*, 3253–3256.
(19) Kadushnikov, R. M.; Skorokhod, V. V.; Kamenin, I. G.; Alievskii, V. M.; Nurkanov, E. Y.; Alievskii, D. M. *Powder Metall. Met. Ceram.* **2001**, *40*, 154–163.
(20) Kirchhof, M. J.; Schmid, H. J.; Peukert, W. *Phys. Rev. E* **2009**, *80*, 026319.
(21) Yadha, V.; Helble, J. J. *J. Aerosol Sci.* **2004**, *35*, 665–681.
(22) Jagota, A.; Dawson, P. R. *Acta Metall.* **1988**, *36*, 2551–2561.
(23) Zhou, H.; Derby, J. J. *J. Am. Ceram. Soc.* **1998**, *81*, 533–540.
(24) Zachariah, M. R.; Carrier, M. J. *J. Aerosol Sci.* **1999**, *30*, 1139–1151.
(25) Hawa, T.; Zachariah, M. R. *Phys. Rev. B* **2007**, *76*, 054109.

dx.doi.org/10.1021/la200546g |*Langmuir* XXXX, XXX, 000–000

(26) Pratsinis, S. E. *AIChE J.* **2010**, 3028–3035.
(27) Rahaman, M. N. *Sintering of Ceramics*; CRC Press: Boca Raton, 2008.
(28) Kuczynski, G. C. *Sintering Processes*; Plenum Press: New York, 1980.
(29) Garabedian, R. S.; Helble, J. J. *J. Colloid Interface Sci.* **2001**, *234*, 248–260.
(30) Tolman, R. C. *J. Chem. Phys.* **1949**, *17*, 333–337.
(31) Jeffrey, A.; Dai, H. H. *Handbook of mathematical formulas and integrals*; Academic Press: Burlington, 2008.
(32) Kobata, A.; Kusakabe, K.; Morooka, S. *AIChE J.* **1991**, *37*, 347–359.
(33) Cazals, F.; Kanhere, H.; Loriot, S. *ACM T. Math. Software* **2011**, 38.
(34) Do Carmo, M. *Differential geometry of curves and surfaces*; Prentice-Hall: Englewood Cliffs, NJ, 1976.
(35) Ryckaert, J. P.; Ciccotti, G.; Berendsen, H. J. C. *J. Comput. Phys.* **1977**, *23*, 327–341.
(36) Forrest, S. R.; Witten, T. A. *J. Phys. A: Math. Gen.* **1979**, *12*, L109–L117.
(37) Jullien, R.; Botet, R. *Aggregation and fractal aggregates*; World Scientific: River Edge, 1987.
(38) Bellehumeur, C. T.; Bisaria, M. K.; Vlachopoulos, J. *Polym. Eng. Sci.* **1996**, *36*, 2198–2207.
(39) Kruis, F. E.; Kusters, K. A.; Pratsinis, S. E.; Scarlett, B. *Aerosol Sci. Technol.* **1993**, *19*, 514–526.
(40) Martinez-Herrera, J. I.; Derby, J. J. *J. Am. Ceram. Soc.* **1995**, *78*, 645–649.
(41) Hawa, T.; Zachariah, M. R. *J. Aerosol Sci.* **2006**, *37*, 1–15.
(42) Hyeon-Lee, J.; Beaucage, G.; Pratsinis, S. E.; Vemury, S. *Langmuir* **1998**, *14*, 5751–5756.
(43) Botet, R.; Jullien, R.; Kolb, M. *J. Phys. A: Math. Gen.* **1984**, *17*, L75–L79.
(44) Sorensen, C. M.; Roberts, G. C. *J. Colloid Interface Sci.* **1997**, *186*, 447–452.
(45) Meakin, P. *J. Sol-Gel Sci. Technol.* **1999**, *15*, 97–117.